

# A Bayesian Approach to Modeling Finite Element Discretization Error

Anne Poot<sup>1</sup> Pierre Kerfriden<sup>2</sup> Iuri Rocha<sup>1</sup> Frans van der Meer<sup>1</sup>

<sup>1</sup>Delft University of Technology, Faculty of Civil Engineering and Geosciences, Delft, the Netherlands

<sup>2</sup>Mines Paris - PSL, Centres des Matériaux, Évry, France

## Abstract

In recent years, there has been a surge of interest in the development of probabilistic approaches to problems that might appear to be purely deterministic. One example of this is the solving of partial differential equations. Since numerical solvers require some approximation of the infinite-dimensional solution space, there is an inherent uncertainty to the solution that is obtained. In this work, the uncertainty associated with the finite element discretization error is modeled following the Bayesian paradigm. First, a continuous formulation is derived, where a Gaussian process prior over the solution space is updated based on observations from a finite element discretization. Due to intractable integrals, a second, finer, discretization is introduced that is assumed sufficiently dense to represent the true solution field. The prior distribution assumed over the fine discretization is then updated based on observations from the coarse discretization. This yields a posterior distribution with a mean close to the deterministic fine-scale solution that is endowed with an uncertainty measure.

The prior distribution over the solution space is defined implicitly by assigning a white noise distribution to the right-hand side. This allows for a sparse representation of the prior distribution, and guarantees that the prior samples have the appropriate level of smoothness for the problem at hand. Special attention is paid to inhomogeneous Dirichlet and Neumann boundary conditions, and how these can be used to enhance this white noise prior distribution. For various problems, we demonstrate how regions of large discretization error are captured in the structure of the posterior standard deviation. The effects of the hyperparameters and observation noise on the quality of the posterior mean and standard deviation are investigated in detail.

# 1 Introduction

In recent years, the Bayesian paradigm has become a popular framework to perform uncertainty quantification. It has found its application in uncertainty propagation, inverse modeling [1] and data assimilation [2] contexts, among others. Commonly, given some numerical model, a prior distribution is assumed over its parameters, and the Bayesian paradigm provides a consistent framework to propagate, estimate or update these uncertain parameters. It should be noted, however, that even if complete certainty could be obtained over the model parameters, there is a remaining uncertainty to the solution due to approximations made in the numerical model. This key observation is what underpins the currently booming field of probabilistic numerics.

At the core of probabilistic numerics, the estimation of some unknown function is recast as a Bayesian inference problem, which allows for the estimation of the function with some uncertainty measure [3, 4]. Early examples of the application of this framework include optimizing functions [5], computing integrals [6] and solving ordinary differential equations [7]. More recently, following a “call to arms” from Hennig et al. [8], a large push has been made to apply this framework to a large range of problems, ranging from solving linear systems [9, 10, 11] to quadrature [12, 13, 14] to solving ordinary differential equations [15, 16, 17]. Most relevant for this work are the probabilistic numerical methods that have been developed for the solving of partial differential equations, which can be roughly divided into two categories: meshfree probabilistic solvers, and solver-perturbing error estimators.

The first category [18, 19, 20] can be seen as a way to find solutions to partial differential equations directly from the strong form. By evaluating the displacement field and its derivatives on a grid of collocation points, a solution can be obtained without needing to apply a finite element discretization over the domain. This approach to solving partial differential equations shares some similarities with Bayesian physics-informed neural networks [21, 22], the main difference lying in the function that is being fitted at the collocation points. The way in which these meshfree solvers relate to traditional collocation methods is similar to the way in which Bayesian physics-informed neural networks relate to their deterministic counterparts.

The second category [23, 24, 25] is more directly focused on estimating the discretization error of traditional solvers for differential equations. For ordinary differential equations, the usual time integration step is taken, after which the solution is perturbed by adding Gaussian noise, representing the uncertainty in the time integration result. Similarly, for partial differential equations, the traditional mesh discretization is perturbed using small support Gaussian random fields, which reflect the uncertainty introduced by the mesh discretization. In [26] and [27], a similar approach is taken, but rather than adding noise to the solution, an uncertainty is introduced by perturbing the time step size or finite element discretization. A more formal mathematical basis for probabilistic numerical methods can be found in [28], where a more rigorous definition of the term is outlined and a common framework underpinning these two seemingly separate categories is established.

It is worth noting that these probabilistic numerical methods are a strong deviation from traditional error estimators [29, 30, 31], as they embed the model error into the method itself, rather than estimate it a posteriori. This inherently affects the model output, which depending on the context can be a desirable or undesirable property. In [32], a method is presented to obtain full-field error estimates by assuming a Gaussian process prior over the discretization error, and updating it based on a set of traditional estimators of error in quantities of interest. This way, a distribution representing the finite element discretization error can be obtained in a non-intrusive manner.

The shared goal of these methods is to accurately describe the errors made due to limitations of our numerical models, though their method of modeling error differs. At the core, the meshfree probabilistic solvers model error as the result of using a finite number of observations to obtain a

solution to an infinite-dimensional problem. The solver-perturbing error estimators, on the other hand, take an existing discretization, like the one used in the finite element method, and assign some uncertainty measure to the existing solver. This prompts us to ask: what happens if the philosophy from the meshfree probabilistic solvers is applied to existing mesh-based solvers of partial differential equations? To the best of our knowledge, beside a brief remark in [33], no attempt has been made to explore the answers to this question.

In this work, we propose a probabilistic numerical method for the modeling of finite element discretization error. The solution is endowed with a Gaussian process prior, which is then updated based on observations of the right-hand side from a finite element discretization. This allows for the approximation of the true solution while including the uncertainty resulting from the finite discretization that is applied. Given the intractability of the exact solution space, it is necessary to introduce a discretization over the domain that is fine enough to represent the exact solution. We present a class of priors that naturally accounts for the smoothness of the partial differential equation at hand, and show how the assembly of large full covariance matrices can be avoided. Special attention is paid to the treatment of Dirichlet and Neumann boundary conditions, and several ways of incorporating boundary information in the prior distribution are presented. The effects of the hyperparameters of the prior distribution as well as observation noise are investigated in detail.

The underlying goal of the development of a Bayesian model for the finite element discretization error, is to enable the propagation of discretization error to quantities of interest through the computational pipelines that arise in multiscale modeling, inverse modeling and data assimilation settings. This consistent treatment of discretization error in turn allows for more informed decisions to be made about its impact on the model output. To give a concrete example, in [34], a Bayesian framework for the assimilation of measurement data and finite element models is presented. Within this framework, a model misspecification component is defined, which is endowed with a squared-exponential Gaussian process prior. The Bayesian formulation of the finite element method that we derive in this work would allow for a more informative choice of prior distribution over the model misspecification component, for example by separating out the discretization error from the error associated with other modeling assumptions.

The outline of this paper is as follows: In Section 2, we derive our Bayesian formulation of the finite element method. This is followed by a discussion on the choice of prior covariance in Section 3, where a class of suitable prior distributions is presented. Then, the results of the method are demonstrated in Section 4 through three different examples: a 1D tapered bar, a 2D L-shaped cantilever, and a 2D porous microstructure. Finally, in Section 5, the conclusions of this paper are drawn and discussed.

## 2 Bayesian Finite Element Method

In this section, our proposed Bayesian version of the finite element method is derived. Although the method is applicable to a large class of partial differential equations, for the purposes of demonstration, we will consider Poisson's equation:

$$\begin{aligned} -\Delta_{\mathbf{x}}u(\mathbf{x}) &= f(\mathbf{x}) && \text{in } \Omega \\ u(\mathbf{x}) &= 0 && \text{on } \partial\Omega \end{aligned} \tag{1}$$

Here,  $\Omega$  and  $\partial\Omega$  are the domain and its boundary, respectively.  $u(\mathbf{x})$  and  $f(\mathbf{x})$  are the solution and forcing term, which are linked through the Laplace operator  $\Delta_{\mathbf{x}}$ .

## 2.1 Continuous formulation

As usual, the problem is restated in its weak formulation:

$$\int_{\Omega} \nabla u(\mathbf{x}) \cdot \nabla v(\mathbf{x}) \, d\mathbf{x} = \int_{\Omega} f(\mathbf{x})v(\mathbf{x}) \, d\mathbf{x} \quad \forall v(\mathbf{x}) \in \mathcal{V} \quad (2)$$

Here,  $\mathcal{V}$  is a Hilbert space of functions over  $\Omega$  that are weakly once-differentiable and vanish at the boundary, and we search  $u(\mathbf{x}) \in \mathcal{V}$ . Now, a discretization is defined over the domain using a set of locally supported shape functions  $\{\psi_i(\mathbf{x})\}_{i=1}^m$ , which span a finite-dimensional space  $\mathcal{W}^h \subset \mathcal{V}$ . The test functions can be defined in terms of these shape functions:

$$v(\mathbf{x}) = \sum_{j=1}^m v_j \psi_j(\mathbf{x}) \quad \text{with } \psi_j(\mathbf{x}) \in \mathcal{W}^h \quad (3)$$

Since Equation (2) has to hold for all  $v(\mathbf{x}) \in \mathcal{W}^h$ , the weights  $v_j$  can be chosen at will. Substituting Equation (3) into Equation (2) and setting  $v_j = \delta_{ij}$ , where  $\delta_{ij}$  is the Kronecker delta function, yields the entries of the finite element force vector  $\mathbf{g}$ :

$$g_i = \int_{\Omega} f(\mathbf{x})\psi_i(\mathbf{x}) \, d\mathbf{x} \quad (4)$$

A centered Gaussian process with a positive definite covariance function  $k(\mathbf{x}, \mathbf{x}')$  is now assumed over the solution  $u(\mathbf{x})$ :

$$u(\mathbf{x}) \sim \mathcal{GP}(0, k(\mathbf{x}, \mathbf{x}')) \quad (5)$$

From Equations (2) to (5), the following covariances between  $u(\mathbf{x})$  and  $f_i$  are obtained:

$$\begin{aligned} \text{cov}(u(\mathbf{x}), u(\mathbf{x}')) &= k(\mathbf{x}, \mathbf{x}') \\ \text{cov}(g_i, u(\mathbf{x}')) &= \int_{\Omega} \nabla_{\mathbf{x}} k(\mathbf{x}, \mathbf{x}') \cdot \nabla_{\mathbf{x}} \psi_i(\mathbf{x}) \, d\mathbf{x} \\ \text{cov}(u(\mathbf{x}), g_j) &= \int_{\Omega} \nabla_{\mathbf{x}'} k(\mathbf{x}, \mathbf{x}') \cdot \nabla_{\mathbf{x}'} \psi_j(\mathbf{x}') \, d\mathbf{x}' \\ \text{cov}(g_i, g_j) &= \int_{\Omega} \int_{\Omega} \nabla_{\mathbf{x}} (\nabla_{\mathbf{x}'} k(\mathbf{x}, \mathbf{x}') \cdot \nabla_{\mathbf{x}'} \psi_j(\mathbf{x}')) \cdot \nabla_{\mathbf{x}} \psi_i(\mathbf{x}) \, d\mathbf{x} \, d\mathbf{x}' \end{aligned} \quad (6)$$

This allows us to define the joint distribution of the solution  $u(\mathbf{x})$  at an arbitrary set of prediction locations  $\mathbf{X}$  and the finite element force vector  $\mathbf{f}$ :

$$\begin{bmatrix} \mathbf{g} \\ u(\mathbf{X}) \end{bmatrix} \sim \mathcal{N}\left(\mathbf{0}, \begin{bmatrix} \text{cov}(\mathbf{g}, \mathbf{g}) & \text{cov}(\mathbf{g}, u(\mathbf{X})) \\ \text{cov}(u(\mathbf{X}), \mathbf{g}) & \text{cov}(u(\mathbf{X}), u(\mathbf{X})) \end{bmatrix}\right) \quad (7)$$

Conditioning now on  $\mathbf{g}$  yields the following posterior distribution:

$$u(\mathbf{X})|\mathbf{g} \sim \mathcal{N}(\mathbf{m}^*, \Sigma^*) \quad (8)$$

Here, the posterior mean vector  $\mathbf{m}^*$  and covariance matrix  $\Sigma^*$  are given by [35]:

$$\begin{aligned} \mathbf{m}^* &= \text{cov}(u(\mathbf{X}), \mathbf{g}) \text{cov}(\mathbf{g}, \mathbf{g})^{-1} \mathbf{g} \\ \Sigma^* &= \text{cov}(u(\mathbf{X}), u(\mathbf{X})) - \text{cov}(u(\mathbf{X}), \mathbf{g}) \text{cov}(\mathbf{g}, \mathbf{g})^{-1} \text{cov}(\mathbf{g}, u(\mathbf{X})) \end{aligned} \quad (9)$$

The posterior mean vector  $\mathbf{m}^*$  provides an estimate of the solution field  $u(\mathbf{x})$  at the prediction locations defined by  $\mathbf{X}$ . The posterior covariance matrix  $\mathbf{\Sigma}^*$  indicates the uncertainty associated with this estimate due to the fact that it was obtained using only a finite set of shape functions. Since the finite discretization is the only source of uncertainty in our model, we can intuitively interpret the posterior covariance as an indicator of finite element discretization error.

Unfortunately, the integrals required to compute the covariances in Equation (6) are generally intractable. For some arbitrary covariance function  $k(\mathbf{x}, \mathbf{x}')$ , the integration over the shape functions  $\psi_i(\mathbf{x})$  and  $\psi_j(\mathbf{x}')$  cannot be performed without putting severe restrictions on which shape functions are permitted. On the other hand, we can design the covariance function such that these integrals do become tractable, for example by following [33] and setting  $k(\mathbf{x}, \mathbf{x}') = G(\mathbf{x}, \mathbf{x}')$ , or following [36] and setting  $k(\mathbf{x}, \mathbf{x}') = \int_{\Omega} \int_{\Omega} G(\mathbf{x}, \mathbf{z})G(\mathbf{x}', \mathbf{z}')\delta(\mathbf{z} - \mathbf{z}')d\mathbf{z}d\mathbf{z}'$ , where  $\delta(\mathbf{x})$  is a Dirac delta function. In both of these expressions, the Green's function  $G(\mathbf{x}, \mathbf{x}')$  associated with the operator  $-\Delta$  is required, which is generally not available for a given partial differential equation. Since our aim is to develop a general Bayesian framework for modeling finite element discretization error, both of these limitations would be unacceptable.

## 2.2 Petrov-Galerkin formulation

This motivates us to approximate  $u(x)$  in the finite-dimensional space  $\mathcal{V}^h$  spanned by a second set of locally supported shape functions  $\{\phi_i(\mathbf{x})\}_{i=1}^n$ :

$$u(\mathbf{x}) = \sum_{i=1}^n u_i \phi_i(\mathbf{x}) \quad (10)$$

Note that this is not the same set of shape functions as the one used to define the force vector in Equation (4). In fact, since our aim is to model the discretization error between  $\mathcal{V}$  and  $\mathcal{W}^h$ , it is important that the error between  $\mathcal{V}$  and  $\mathcal{V}^h$  is negligible compared to the error between  $\mathcal{V}^h$  and  $\mathcal{W}^h$ . Since  $\mathcal{W}^h \neq \mathcal{V}^h$ , our Bayesian formulation of the finite element method is a Petrov-Galerkin method, as opposed to the usual Bubnov-Galerkin method, where the test and trial functions come from the same space.

Substituting Equations (3) and (10) into Equation (2) yields the matrix formulation of the problem:

$$\mathbf{H}\mathbf{u} = \mathbf{g} \quad (11)$$

Note that the elements of the force vector  $\mathbf{g}$  are still the same as in Equation (4). The elements of the stiffness matrix  $\mathbf{H}$  are given by:

$$H_{ij} = \int_{\Omega} \nabla \phi_i(\mathbf{x}) \cdot \nabla \psi_j(\mathbf{x}) d\mathbf{x} \quad (12)$$

Since the solution field  $u(x)$  has been reduced from the infinite-dimensional space  $\mathcal{V}$  to the finite-dimensional  $\mathcal{V}^h$ , the distribution assumed over the solution in Equation (5) needs to be reduced accordingly. Instead of an infinite-dimensional Gaussian process, we obtain a finite-dimensional zero-mean normal distribution with a positive definite covariance matrix  $\mathbf{\Sigma}$ :

$$\mathbf{u} \sim \mathcal{N}(0, \mathbf{\Sigma}) \quad (13)$$

The joint distribution of  $\mathbf{u}$  and  $\mathbf{g}$  is now given by:

$$\begin{bmatrix} \mathbf{g} \\ \mathbf{u} \end{bmatrix} = \begin{bmatrix} \mathbf{H}\mathbf{u} \\ \mathbf{u} \end{bmatrix} \sim \mathcal{N}\left(0, \begin{bmatrix} \mathbf{H}\mathbf{\Sigma}\mathbf{H}^T & \mathbf{H}\mathbf{\Sigma} \\ \mathbf{\Sigma}\mathbf{H}^T & \mathbf{\Sigma} \end{bmatrix}\right) \quad (14)$$

Conditioning  $\mathbf{u}$  on  $\mathbf{g}$  yields the following posterior distribution:

$$\mathbf{u}|\mathbf{g} \sim \mathcal{N}(\mathbf{m}^*, \mathbf{\Sigma}^*) \quad (15)$$

Here, the posterior mean vector  $\mathbf{m}^*$  and covariance matrix  $\mathbf{\Sigma}^*$  are given by:

$$\begin{aligned} \mathbf{m}^* &= \mathbf{\Sigma} \mathbf{H}^T \left( \mathbf{H} \mathbf{\Sigma} \mathbf{H}^T \right)^{-1} \mathbf{g} \\ \mathbf{\Sigma}^* &= \mathbf{\Sigma} - \mathbf{\Sigma} \mathbf{H}^T \left( \mathbf{H} \mathbf{\Sigma} \mathbf{H}^T \right)^{-1} \mathbf{H} \mathbf{\Sigma} \end{aligned} \quad (16)$$

Similar to the continuous formulation presented in section 2.1,  $\mathbf{m}^*$  can be interpreted as providing an estimate of the solution  $u(\mathbf{x})$  in the fine space  $\mathcal{V}^h$ , while observing the right-hand side  $f(\mathbf{x})$  only in the coarse space  $\mathcal{W}^h$ . The posterior covariance matrix  $\mathbf{\Sigma}^*$  then provides an indication of the uncertainty associated with this estimate due to the limited number of observations that are being made, which can be taken as an indicator of finite element discretization error. Note that if the Bubnov-Galerkin formulation (i.e.  $\mathcal{W}^h = \mathcal{V}^h$ ) was used,  $\mathbf{\Sigma}^*$  would reduce to a null matrix, reflecting the fact that there no longer exists a discretization error between  $\mathcal{V}^h$  and  $\mathcal{W}^h$ .

### 2.3 Hierarchical shape functions

Thus far, the only requirement that has been put on the choice of  $\mathcal{V}^h$  and  $\mathcal{W}^h$ , is that the error between  $\mathcal{V}$  and  $\mathcal{V}^h$  is negligible compared to the error between  $\mathcal{V}^h$  and  $\mathcal{W}^h$ . We now add a second restriction, and assume that  $\mathcal{W}^h \subset \mathcal{V}^h$ . This defines a hierarchy between these two spaces, and implies that any function defined in  $\mathcal{W}^h$  can be expressed in  $\mathcal{V}^h$ . One way to ensure this hierarchy in practice is to first define a coarse mesh corresponding to  $\mathcal{W}^h$ , and then refine it to obtain a fine mesh corresponding to  $\mathcal{V}^h$ . Alternatively, it is possible to use only a single mesh, and use linear and quadratic shape functions to define the  $\mathcal{V}^h$  and  $\mathcal{W}^h$ , respectively.

From the hierarchy between  $\mathcal{V}^h$  and  $\mathcal{W}^h$ , it follows that the basis functions that span the coarse space  $\mathcal{W}^h$  can be written as a linear combination of the basis functions that span the fine space  $\mathcal{V}^h$ . In other words, there exists a matrix<sup>1</sup>  $\mathbf{\Phi}^T$  that maps a vector of fine shape functions  $\boldsymbol{\phi}(\mathbf{x}) = [\phi_1(\mathbf{x}) \phi_2(\mathbf{x}) \dots \phi_n(\mathbf{x})]^T$  to a vector of coarse shape functions  $\boldsymbol{\psi}(\mathbf{x}) = [\psi_1(\mathbf{x}) \psi_2(\mathbf{x}) \dots \psi_m(\mathbf{x})]^T$ :

$$\boldsymbol{\psi}(\mathbf{x}) = \mathbf{\Phi}^T \boldsymbol{\phi}(\mathbf{x}) \quad (17)$$

This allows Equation (12) to be rewritten as:

$$H_{ij} = \int_{\Omega} \nabla \sum_{k=1}^n \Phi_{ki} \phi_k(\mathbf{x}) \cdot \nabla \phi_j(\mathbf{x}) \, d\mathbf{x} = \sum_{k=1}^n \Phi_{ki} \int_{\Omega} \nabla w_k(\mathbf{x}) \cdot \nabla \phi_j(\mathbf{x}) \, d\mathbf{x} \quad (18)$$

As a result,  $\mathbf{H}$  can be expressed as:

$$\mathbf{H} = \mathbf{\Phi}^T \mathbf{K} \quad (19)$$

where  $\mathbf{K}$  is the Bubnov-Galerkin stiffness matrix if both trial and test functions came from the fine space  $\mathcal{V}^h$ :

$$K_{ij} = \int_{\Omega} \nabla \phi_i(\mathbf{x}) \cdot \nabla \phi_j(\mathbf{x}) \, d\mathbf{x} \quad (20)$$

---

<sup>1</sup>Note that  $\mathbf{\Phi}$  has been defined in terms of its transpose in order to make expressions in later sections consistent with common notation for least squares, proper orthogonal decomposition, and so on.

In a similar way, Equation (4) can be rewritten as:

$$g_i = \int_{\Omega} f(x) \sum_{k=1}^n \Phi_{ki} \phi_k(\mathbf{x}) \, d\mathbf{x} = \sum_{k=1}^n \Phi_{ki} \int_{\Omega} f(x) \phi_k(\mathbf{x}) \, d\mathbf{x} \quad (21)$$

And so,  $\mathbf{g}$  can be expressed as:

$$\mathbf{g} = \mathbf{\Phi}^T \mathbf{f} \quad (22)$$

where  $\mathbf{f}$  is the force vector the test functions came from the fine space  $\mathcal{V}^h$ :

$$f_i = \int_{\Omega} f(\mathbf{x}) \phi_i(\mathbf{x}) \, d\mathbf{x} \quad (23)$$

These relationships will prove useful later on, and are in fact the main motivation for choosing the shape functions in a hierarchical manner.

Finally, we define the reference solution  $\hat{\mathbf{u}}$  as the solution to the fine-scale system of equations that follows from the fine-scale Bubnov-Galerkin formulation:

$$\mathbf{K} \hat{\mathbf{u}} = \mathbf{f} \quad (24)$$

In the remainder of this work, discretization error is defined with respect to  $\hat{\mathbf{u}}$ , unless specified otherwise.

## 2.4 Boundary conditions

It is worth considering how the application of boundary conditions in the fine space translates to the shape functions in the coarse space. To do this,  $\phi(\mathbf{x})$  is split into  $\phi_i(\mathbf{x})$  and  $\phi_d(\mathbf{x})$ . This could be considered abuse of notation, since  $\mathcal{V}^h \in \mathcal{V}$ , which is already constrained by the Dirichlet boundary conditions, so from this point of view,  $\phi_d(\mathbf{x})$  should not exist. However, in most practical finite element implementations, shape functions are assigned to the boundary nodes as well, in order to facilitate the inclusion of inhomogeneous boundary conditions in the model.

The boundary conditions in the coarse space follow from  $\phi_d(\mathbf{x})$  and  $\mathbf{\Phi}$ :  $\psi_d(\mathbf{x})$  is defined as the elements of  $\psi(\mathbf{x})$  where the rows of  $\mathbf{\Phi}$  belonging to  $\phi_d(\mathbf{x})$  have non-zero entries. As a result, Equation (19) can be split as follows:

$$\begin{bmatrix} \psi_i(\mathbf{x}) \\ \psi_d(\mathbf{x}) \end{bmatrix} = \begin{bmatrix} \mathbf{\Phi}_{ii}^T & \mathbf{0} \\ \mathbf{\Phi}_{id}^T & \mathbf{\Phi}_{dd}^T \end{bmatrix} \begin{bmatrix} \phi_i(\mathbf{x}) \\ \phi_d(\mathbf{x}) \end{bmatrix} \quad (25)$$

Note that the fact that  $\mathbf{\Phi}_{di} = \mathbf{0}$  does not introduce any loss of generality: any non-zero element of  $\mathbf{\Phi}_{di}$  would by definition of  $\psi_d(\mathbf{x})$  be an element of  $\mathbf{\Phi}_{dd}$ , not  $\mathbf{\Phi}_{di}$ . From Equations (19) and (25), it follows that:

$$\mathbf{H}_{ii} = \mathbf{\Phi}_{ii}^T \mathbf{K}_{ii} \quad (26)$$

Similarly, from Equations (22) and (25), it follows that:

$$\mathbf{g}_i = \mathbf{\Phi}_{ii}^T \mathbf{f}_i \quad (27)$$

Commonly, Dirichlet boundary conditions are enforced by eliminating the corresponding degrees of freedom, and solving the system that remains. Due to the simple relation that  $\mathbf{\Phi}_{ii}$  provides between  $\mathbf{H}_{ii}$  and  $\mathbf{K}_{ii}$  (Equation (26)) as well as  $\mathbf{g}_i$  and  $\mathbf{f}_i$  (Equation (27)), all relationships described in Sections 2.2 and 2.3 still hold when applied to only the internal nodes of the system. From this

point onward, we will therefore only consider the internal nodes of the system. This also means that only the part of the covariance matrix related to the internal nodes  $\Sigma_{\mathbf{ii}}$  needs to be considered, and so the requirement of positive definiteness of  $\Sigma$  can be relaxed to a requirement of positive definiteness of only  $\Sigma_{\mathbf{ii}}$ . The subscripts  $\mathbf{i}$  (for vectors) and  $\mathbf{ii}$  (for matrices) will be left implied in order to declutter the notation.

### 3 Choice of Prior Covariance

Thus far, the prior covariance matrix  $\Sigma$  has not been specified. The choice of  $\Sigma$  is subject to two main requirements. The first requirement is that  $\Sigma$  needs to have a sparse representation. Since  $\Sigma$  is a full  $n \times n$  matrix, where  $n$  is the number of degrees of freedom of the fine discretization, explicitly computing, storing and applying operations on it would quickly become prohibitively expensive. As a result, the traditional approach of using a kernel to directly compute all entries of  $\Sigma$  would be infeasible. Instead, a stochastic partial differential equation is used to define the prior distribution, without needing to explicitly compute  $\Sigma$ . For certain kernel-based priors, an equivalent stochastic partial differential equation can be shown to exist, see for example [37].

The second requirement is that the choice of prior distribution needs to be appropriate for the partial differential equation at hand. For instance, if the infinitely differentiable squared exponential prior were assumed on the solution field  $u(x)$ , this would imply  $C^\infty$  continuity on the right-hand side field  $f(x)$ , which is usually an undesirable assumption to make. On the other hand, if the prior is not smooth enough, samples from the prior would exhibit unphysical discontinuities in  $u(x)$  or its gradient fields. In short, the prior needs to respect the smoothness of the partial differential equation to which it is applied.

In this section, a particular class of priors that meets both of these requirements is presented.

#### 3.1 A sparse right-hand side prior

Following the approach taken in [19], rather than assuming a prior measure directly on the displacement field  $u(\mathbf{x})$ , we assume a centered Gaussian process prior with covariance function  $k_f(\mathbf{x}, \mathbf{x}')$  over the forcing term  $f(\mathbf{x})$ :

$$f(\mathbf{x}) \sim \mathcal{GP}(0, k_f(\mathbf{x}, \mathbf{x}')) \quad (28)$$

This implicitly defines an equivalent prior on  $u(\mathbf{x})$ :

$$u(\mathbf{x}) \sim \mathcal{GP}(0, k_{\text{nat}}(\mathbf{x}, \mathbf{x}')) \quad (29)$$

Here, the covariance function  $k_{\text{nat}}$  can be expressed in terms of  $k_f(\mathbf{x}, \mathbf{x}')$  and the Green's function  $G(\mathbf{x}, \mathbf{x}')$  associated with the operator of the partial differential equation:

$$k_{\text{nat}}(\mathbf{x}, \mathbf{x}') = \int_{\Omega} \int_{\Omega} G(\mathbf{x}, \mathbf{z}) G(\mathbf{x}', \mathbf{z}') k_f(\mathbf{z}, \mathbf{z}') d\mathbf{z} d\mathbf{z}' \quad (30)$$

In [19], this kernel is described as “natural” in the sense that the operator  $-\Delta$  (see Equation (1)) uniquely maps from the Hilbert space associated with the forcing term covariance function  $k(\mathbf{x}, \mathbf{x}')$  to the one associated with  $k_{\text{nat}}(\mathbf{x}, \mathbf{x}')$ . Each sample from  $u(\mathbf{x})$  drawn from this natural kernel has an equivalent sample from  $f(\mathbf{x})$  and vice versa. Unfortunately, since the Green's function is generally not available for a given partial differential equation, in practical cases this natural kernel is then discarded in favor of a Matérn or Wendland kernel with the appropriate level of smoothness.

However, an important distinction between [19] and this work is that we are concerned with the finite element method rather than collocation methods. As a result, it is not necessary to step away



from the natural prior approach. Instead, it can be approximated by applying the finite element discretization first, and only then finding the natural covariance matrix for the solution vector  $\mathbf{u}$ . Given the prior distribution over  $f(\mathbf{x})$  in Equation (28) and the definition of the force vector in Equation (20), it follows that:

$$\mathbf{f} \sim \mathcal{N}(\mathbf{0}, \Sigma_f) \quad (31)$$

where the force vector covariance matrix  $\Sigma_f$  is given by:

$$\Sigma_f = \int_{\Omega} \int_{\Omega} \mathbf{w}(\mathbf{x}) k_f(\mathbf{x}, \mathbf{x}') \mathbf{w}(\mathbf{x}')^T d\mathbf{x}' d\mathbf{x} \quad (32)$$

The resulting prior distribution over  $\mathbf{u}$  then becomes:

$$\mathbf{u} \sim \mathcal{N}(\mathbf{0}, \mathbf{K}^{-1} \Sigma_f \mathbf{K}^{-1}) \quad (33)$$

Note the similarity to the natural kernel in Equation (30), with  $\mathbf{K}^{-1}$  and  $\Sigma_f$  taking a similar role as  $G(\mathbf{x}, \mathbf{x}')$  and  $k_f(\mathbf{x} - \mathbf{x}')$ , respectively [38]. Also similarly, each sample from  $\mathbf{u}$  has an equivalent sample from  $\mathbf{f}$  and vice versa. Conceptually, our approach is the same as [19], except that we are working in the finite-dimensional space of the discretized system, rather than the infinite-dimensional space of the original partial differential equation. The advantage of working in the finite-dimensional space is that  $\mathbf{K}^{-1}$  is computable, and as a result the natural prior can still be used.

Given this choice of prior and using Equation (19), the posterior distribution of the displacement field is given by:

$$\mathbf{u} | \mathbf{g} \sim \mathcal{N}(\mathbf{m}^*, \Sigma^*) \quad (34)$$

with the following posterior mean  $\mathbf{m}^*$  and posterior covariance  $\Sigma^*$ :

$$\begin{aligned} \mathbf{m}^* &= \mathbf{K}^{-1} \Sigma_f \Phi \left( \Phi^T \Sigma_f \Phi \right)^{-1} \Phi^T \mathbf{f} \\ \Sigma^* &= \mathbf{K}^{-1} \left( \mathbf{I} - \Sigma_f \Phi \left( \Phi^T \Sigma_f \Phi \right)^{-1} \Phi^T \right) \Sigma_f \mathbf{K}^{-1} \end{aligned} \quad (35)$$

The posterior mean is similar to the reference solution  $\hat{\mathbf{u}}$ , except that the force vector  $\mathbf{f}$  has been replaced by  $\hat{\mathbf{f}}$ , a weighted projection onto the column space of  $\Phi$ :

$$\hat{\mathbf{f}} = \mathbf{P} \mathbf{f} = \Sigma_f \Phi \left( \Phi^T \Sigma_f \Phi \right)^{-1} \Phi^T \mathbf{f} \quad (36)$$

This projected force vector  $\hat{\mathbf{f}}$  and associated projection matrix  $\mathbf{P}$  can also be interpreted as the solution to the following generalized least squares problem, where the error term  $\epsilon$  has a precision matrix  $\Sigma_f$ :

$$\mathbf{f} = \Phi \mathbf{g} + \epsilon \quad (37)$$

From this point of view, we can also make sense of the posterior covariance by relating it to the residual maker matrix  $\mathbf{Q} = \mathbf{I} - \mathbf{P}$  associated with the generalized least squares problem given in Equation (37):

$$\Sigma^* = \mathbf{K}^{-1} \mathbf{Q} \Sigma_f \mathbf{K}^{-1}, \quad (38)$$

If no information was lost when projecting  $\mathbf{f}$  onto the coarse space and back, then the posterior mean  $\mathbf{m}^*$  would be exactly equal to the reference solution  $\hat{\mathbf{u}}$ , and  $\mathbf{Q}$  and  $\Sigma^*$  reduce to null matrices. Generally, however, this projection between the fine and coarse space will introduce loss of information, due to the fact that the coarse shape functions do not have the same expressivity as the fine shape functions. The lack of expressivity is in fact the root cause of discretization errors in the first place, so it is worth emphasizing that this is being reflected in the posterior covariance.

### 3.2 White noise prior

Within the natural prior framework, the main choice that remains is what right-hand side covariance function  $k_f(\mathbf{x}, \mathbf{x}')$  to assume. In this paper, we will mostly follow [19] and [36], and assume  $k_f(\mathbf{x}, \mathbf{x}')$  to be a Dirac delta function  $\delta(\mathbf{x})$ , scaled by a single hyperparameter  $\alpha$ :

$$k_f(\mathbf{x}, \mathbf{x}') = \alpha^2 \delta(\mathbf{x} - \mathbf{x}') \quad (39)$$

This defines a white noise field over  $f(\mathbf{x})$  with a standard deviation that is equal to  $\alpha$ . The covariance matrices  $\Sigma_f$  and  $\Sigma$  then follow directly from Equations (32) and (33):

$$\begin{aligned} \Sigma_f &= \alpha^2 \mathbf{M} \\ \Sigma &= \alpha^2 \mathbf{K}^{-1} \mathbf{M} \mathbf{K}^{-1} \end{aligned} \quad (40)$$

where  $\mathbf{M}$  is the classic Bubnov-Galerkin mass matrix, given by:

$$M_{ij} = \int_{\Omega} w_i(\mathbf{x}) w_j(\mathbf{x}) d\mathbf{x} \quad (41)$$

Note that under this choice of prior covariance, the sparsity requirement that was put on  $\Sigma$  has been met.

The resulting posterior mean vector and covariance matrix are then given by:

$$\begin{aligned} \mathbf{m}^* &= \mathbf{K}^{-1} \mathbf{M} \Phi \left( \Phi^T \mathbf{M} \Phi \right)^{-1} \Phi^T \mathbf{f} \\ \Sigma^* &= \alpha^2 \mathbf{K}^{-1} \left( \mathbf{I} - \mathbf{M} \Phi \left( \Phi^T \mathbf{M} \Phi \right)^{-1} \Phi^T \right) \mathbf{M} \mathbf{K}^{-1} \end{aligned} \quad (42)$$

It can be seen that for this choice of prior, the hyperparameter  $\alpha$  does not affect the posterior mean, and directly scales the posterior covariance. Additionally, the contraction matrix  $\mathbf{C}$  presented in Equation (45) is also hyperparameter-independent.

### 3.3 Hyperparameter tuning

For the tuning of the single hyperparameter  $\alpha$ , several approaches could be considered. One common approach in the Bayesian framework is to maximize the marginal likelihood of the observed data. In our case, the log marginal likelihood of the observation vector  $\mathbf{g}$  is given by:

$$\log p(\mathbf{g}) = -\frac{1}{2\alpha^2} \mathbf{g}^T \left( \Phi^T \mathbf{M} \Phi \right)^{-1} \mathbf{g} - n \log \alpha - \frac{1}{2} \log \left| \Phi^T \mathbf{M} \Phi \right| - \frac{n}{2} \log 2\pi \quad (43)$$

Taking the derivative with respect to  $\alpha$  and setting it equal to 0 yields the following closed-form expression for the maximum likelihood estimate:

$$\alpha_{\text{MLE}} = \sqrt{\frac{1}{n} \mathbf{g}^T \left( \Phi^T \mathbf{M} \Phi \right)^{-1} \mathbf{g}} \quad (44)$$

Another option is to estimate the difference between reference solution  $\hat{\mathbf{u}}$  and the posterior mean  $\mathbf{m}^*$  based on the posterior distribution, and then scale  $\alpha$  accordingly. To obtain such an estimate, we first define the contraction matrix  $\mathbf{C}$ :

$$\mathbf{C} = \Sigma^* \Sigma^{-1} = \mathbf{I} - \mathbf{K}^{-1} \Sigma_f \Phi \left( \Phi^T \Sigma_f \Phi \right)^{-1} \Phi^T \mathbf{K} \quad (45)$$

Note that  $\mathbf{C}$  does not depend on  $\alpha$ . This matrix can be interpreted as an indicator of the shrinkage of the posterior covariance relative to the prior covariance, due to the data that was observed. Postmultiplying by the reference solution  $\hat{\mathbf{u}}$ , we find exactly the difference between the reference solution  $\hat{\mathbf{u}}$  and the posterior mean  $\mathbf{m}^*$ :

$$\mathbf{C}\hat{\mathbf{u}} = \hat{\mathbf{u}} - \mathbf{K}^{-1}\Sigma_f\Phi\left(\Phi^T\Sigma_f\Phi\right)^{-1}\mathbf{g} = \hat{\mathbf{u}} - \mathbf{m}^* \quad (46)$$

This might not appear useful, as the reference solution  $\hat{\mathbf{u}}$  is not known beforehand. However,  $\mathbf{C}\hat{\mathbf{u}}$  can cheaply be approximated, provided that  $\Sigma_f^{-1}$  can be cheaply approximated, for example by diagonalizing  $\Sigma_f$ . In this case,  $\Sigma^*$  can be approximated through sampling, as explained in Appendix A, and the other terms are known matrices and vectors:

$$\mathbf{C}\hat{\mathbf{u}} = \Sigma^*\mathbf{K}\Sigma_f^{-1}\mathbf{f} \quad (47)$$

This estimate of the difference between  $\hat{\mathbf{u}}$  and  $\mathbf{m}^*$  can then be used tune  $\alpha$  appropriately [38].

### 3.4 Enrichment of the prior covariance

One potential drawback of the white noise prior presented here is that its posterior covariance is load-independent. Since the locations of strain concentrations, singularities and largest discretization error often depend on the combination of geometry and load, it can be beneficial to explicitly model this dependency through an additional term in the prior covariance. In Section 2.4, only homogeneous Dirichlet boundary conditions were considered. Here, we expand on this and demonstrate how both homogeneous and inhomogeneous Dirichlet and Neumann boundary conditions can be included in the model. This is accomplished by assigning a statistically independent normal distribution to the displacement along the Dirichlet boundary  $\mathbf{u}_d$ , as well as the force along the Neumann boundary  $\mathbf{f}_n$ :

$$\mathbf{u}_d \sim \mathcal{N}(\mathbf{m}_d, \beta^2\Sigma_d) \quad \mathbf{f}_n \sim \mathcal{N}(\mathbf{m}_n, \gamma^2\Sigma_n) \quad (48)$$

The assignment of these prior distributions to the Dirichlet and Neumann boundary conditions produces the following prior mean and covariance of the forcing term:

$$\begin{aligned} \mathbf{m}_f &= \mathbf{K}_{id}\mathbf{m}_d + \mathbf{m}_f \\ \Sigma_f &= \alpha^2\mathbf{M} + \beta^2\mathbf{K}_{id}\Sigma_d\mathbf{K}_{id}^T + \gamma^2\Sigma_n \end{aligned} \quad (49)$$

By adjusting  $\beta$  and  $\gamma$ , the effects of particular loads can be emphasized or de-emphasized.

This generalization allows for a modeling choice when enforcing inhomogeneous Dirichlet boundary conditions. These can be strongly enforced in the prior, by setting  $\Sigma_d = \mathbf{0}$  and making  $\mathbf{m}_d$  equal to the true displacement value at the boundary. Alternatively, they can be weakly enforced by setting  $\mathbf{m}_d = \mathbf{0}$ , and instead assigning a non-zero covariance  $\Sigma_d$ . In this case, the Dirichlet boundaries are enforced in a weak sense, because their enforcement is only due to the right-hand side modifications being included in the observations. Naturally, a combination of these two approaches, where both  $\mathbf{m}_d$  and  $\Sigma_d$  are non-zero is also valid. For homogeneous Dirichlet boundary conditions, setting  $\mathbf{m}_d = \mathbf{0}$  and  $\Sigma_d = \mathbf{0}$  already strongly enforces the boundary conditions, but this strong enforcement can be weakened by introducing a non-zero  $\Sigma_d$ . For Neumann boundary conditions, the same modeling choice between strong and weak enforcement of the boundary conditions applies.

A final point to address is which covariance structure should be applied to the Dirichlet and Neumann covariances  $\Sigma_d$  and  $\Sigma_n$ . For single point loads and single point constraints, the answer

to this question is trivial, namely a null matrix, except for a unit diagonal entry associated with the point load or constraint degree of freedom. If the problem contains multiple independent point loads or constraints, the covariance structure of  $\Sigma_d$  and  $\Sigma_n$  is still relatively straightforward: in this case, the off-diagonal terms of  $\Sigma_d$  and  $\Sigma_n$  can simply be set to 0. However, if for example an inhomogeneous Dirichlet or Neumann boundary condition is applied along an edge, this assumption of independence does not hold, and a full covariance structure needs to be obtained for  $\Sigma_d$  and  $\Sigma_n$ .

### 3.5 Observation noise

It is common in Gaussian process regression model to include a certain amount of observation noise in the model. In general, the inclusion of observation noise increases the relative importance of the prior compared to the observed data. This can be beneficial if the data has been obtained from noisy measurements, or as a form of regularization to prevent overfitting. It can also be the case that useful features of the prior distribution vanish from the posterior distributions, because they are drowned out by the observation. By introducing observation noise, the observed data is prevented from dominating the problem, and such features can still be propagated to the posterior.

If i.i.d. observation noise with magnitude  $\sigma_e$  is included in the model, the posterior mean vector and covariance matrix given in Equation (42) become:

$$\begin{aligned} m^* &= \alpha^2 \mathbf{K}^{-1} \mathbf{M} \Phi \left( \alpha^2 \Phi^T \mathbf{M} \Phi + \sigma_e^2 \mathbf{I} \right)^{-1} \mathbf{g} \\ \Sigma^* &= \mathbf{K}^{-1} \left( \alpha^2 \mathbf{M} - \alpha^4 \mathbf{M} \Phi \left( \alpha^2 \Phi^T \mathbf{M} \Phi + \sigma_e^2 \mathbf{I} \right)^{-1} \Phi^T \mathbf{M} \right) \mathbf{K}^{-1} \end{aligned} \quad (50)$$

Note that several previously demonstrated relationships no longer hold if observation noise is added to the model. This includes the analogy with the generalized least squares problem in Equation (37), as well as the exact maximum likelihood estimate in Equation (44).

## 4 Results

### 4.1 1D tapered bar

The following one-dimensional mechanics problem with inhomogeneous Dirichlet boundary conditions is considered:

$$\begin{aligned} -\frac{d}{dx} \left( k(x) \frac{du}{dx} \right) &= f(x) & \text{in } \Omega = (0, 1) \\ u(x) &= 0 & \text{on } x = 0 \\ u(x) &= 1 & \text{on } x = 1 \end{aligned} \quad (51)$$

Here,  $f(x) = 1$  and  $k(x) = 1 - 0.9x$ . This setup describes a tapered bar with a constant load, where the left end is clamped and a unit displacement is prescribed on the right end. The coarse and fine discretization consist of a uniform mesh of 4 linear elements and 64 linear elements, respectively. Note that this means that each coarse element is subdivided into 16 fine elements, and as a result, the hierarchy between the shape function spaces described in Section 2.2 is ensured. The white noise prior distribution presented in Section 3.2 is assumed, with  $\alpha = 1$ . In order to ensure that the observation covariance matrix is positive definite, a small observation noise ( $\sigma_e = 10^{-8}$ ) is added to the model. The inhomogeneous Dirichlet boundary conditions are treated deterministically, as described in Section 2.4.

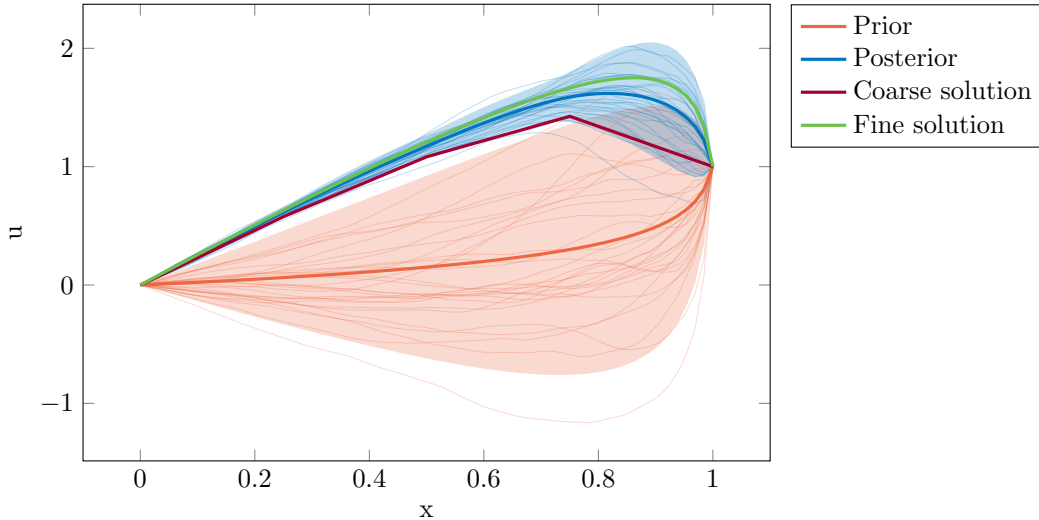


Figure 1: Prior and posterior distributions of the 1D tapered bar problem. For comparison, the fine-scale and coarse-scale reference solutions have been included. From each distribution, 30 samples have been plotted. The shaded regions correspond to the 95% confidence intervals of the distributions.

In Figure 1, the resulting prior and posterior distribution is shown. Several pieces of information about the problem, in absence of knowledge of the right-hand side term, can be found encoded in the prior. The Dirichlet boundary conditions at  $x = 0$  and  $x = 1$  have been accounted for in the prior mean with a standard deviation of 0 at those locations. The prior mean corresponds to the displacement field of the bar under Dirichlet boundary conditions alone. Furthermore, a larger prior standard deviation is found in the region where the bar is thinner, reflecting the fact that a small perturbation in the right-hand side in this region would have a significant effect on the displacement field. Considering the posterior distribution, we see that its mean falls between the coarse- and fine-scale reference solutions. Lastly, it can be seen that the region where the posterior standard deviation is largest corresponds to the region where the discretization error is largest.

In Figure 2, we increase the number of degrees of freedom of the coarse mesh  $n_c$  to study its effect on the posterior distribution. As the coarse-scale solution approaches the fine-scale solution, the posterior mean approaches the fine-scale solution accordingly. Additionally, the posterior standard deviation shrinks along with the discretization error until the coarse mesh density meets the fine one at  $n_c = n_f = 64$ . At this point, only a small posterior standard deviation remains due to the small observation noise that was included in the model.

## 4.2 2D L-shaped cantilever

For a two-dimensional example, the L-shaped cantilever beam problem shown in Figure 3 is considered. For this particular problem, it is well known that a singularity occurs at the inner corner of the beam. This, in turn, produces a large discretization error in the strain field at this location. For this reason, this example will be focused on the strain field  $\boldsymbol{\varepsilon}(\boldsymbol{x})$ . The strain field can be sampled by simply sampling the solution  $\boldsymbol{u}$  as described in Appendix A, and then computing the corresponding

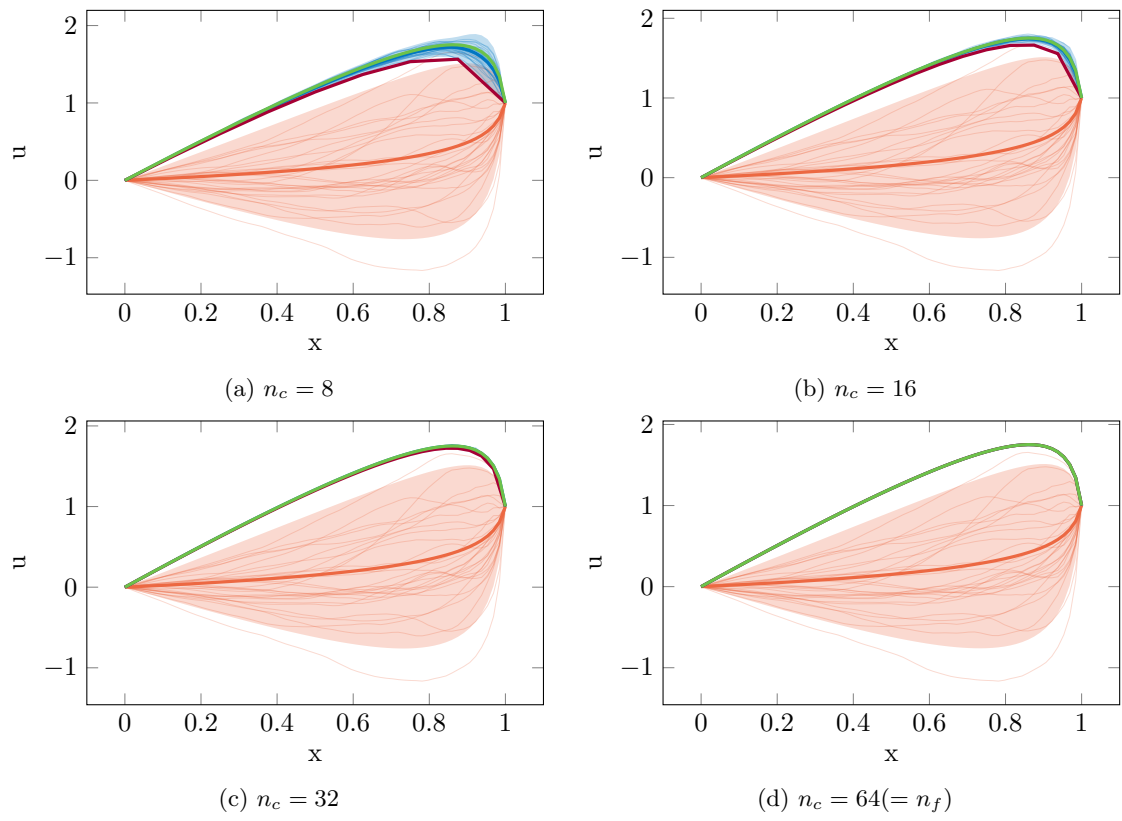


Figure 2: Evolution of the posterior distribution as the number of coarse-scale degrees of freedom  $n_c$  increases towards the number of fine-scale degrees of freedom  $n_f$ .

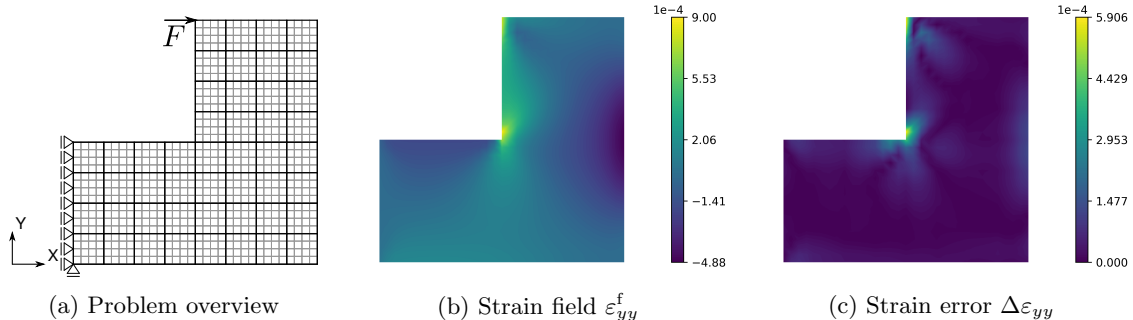


Figure 3: The vertical strain field and corresponding discretization error of the L-shaped cantilever problem

strain field for each sample. Both the coarse and fine mesh consist of quadrilateral elements with linear shape functions, as shown in Figure 3a. The elements of the coarse and fine mesh have a side length  $h_c = 0.25$  and  $h_f = 0.0625$ , respectively. For this example, linear elasticity under small strains and plane stress conditions is assumed. In Figure 3b, the strain field associated with the reference solution  $\varepsilon_{yy}^f$  is shown. The error in the strain field between the coarse and fine discretization  $\Delta\varepsilon_{yy} = |\varepsilon_{yy}^f - \varepsilon_{yy}^c|$  is shown in Figure 3c.

Since the stress concentration arises due to a combination of loading conditions and geometry, it might be desirable to amplify the effects of the loading conditions in the prior. To this end, the white noise prior used thus far is enriched by an additional term representing the uncertainty due to the Neumann boundary condition  $\mathbf{f}_n$ :

$$\Sigma_{\mathbf{f}} = \alpha^2 \mathbf{M} + \gamma^2 \Sigma_{\mathbf{n}} \quad (52)$$

Here,  $\Sigma_{\mathbf{n}}$  is the covariance matrix associated with the inhomogeneous Neumann boundary degrees of freedom. Since in this case only a single point load is applied,  $\Sigma_{\mathbf{n}}$  is a null matrix, except for a unit diagonal entry associated with the point load degree of freedom. With the definition of the prior in Equation (52),  $\alpha$  controls the effect of the geometry under general loading conditions on the discretization error, while  $\gamma$  controls the effect of the point load specifically.

Before moving to a more general setting, we first consider two extreme cases for the hyperparameter values, namely  $(\alpha, \gamma) = (1, 0)$  and  $(\alpha, \gamma) = (0, 1)$ . The observation noise is set to a small value ( $\sigma_e = 10^{-8}$ ), so the prior and posterior distributions represent the limit cases of  $\sigma_e \rightarrow \infty$  and  $\sigma_e \rightarrow 0$ , respectively. To ensure positive definiteness for the  $(\alpha, \gamma) = (0, 1)$  case, a small white noise with magnitude  $\sigma = 10^{-6}$  is added to the diagonal of the covariance matrix. In Figure 4, the prior and posterior standard deviations of the vertical strain field  $\varepsilon_{yy}$  are plotted for both cases.

It can be observed that in the prior distribution, the singularity is activated in both cases, although it is more pronounced for  $(\alpha, \gamma) = (0, 1)$ , as intended. In the posterior distributions, however, this information appears to vanish, and an essentially uniform standard deviation appears in both strain fields. For the purposes of modeling discretization error, this lack of regions of interest from the posterior distribution is undesirable. However, this problem can be mitigated by increasing the amount of observation noise  $\sigma_e$  in our model. From a Bayesian perspective, this can be seen as an increase of the importance of the prior distribution relative to the observed data.

In order to better understand the interplay between  $\alpha$ ,  $\gamma$  and  $\sigma_e$ , it is useful to consider the ratios  $\frac{\gamma}{\alpha}$  and  $\frac{\sigma_e}{\alpha}$  instead of the complete set of hyperparameters. This way, the structure of the posterior standard deviation is decoupled from its magnitude: the structure can be tuned with

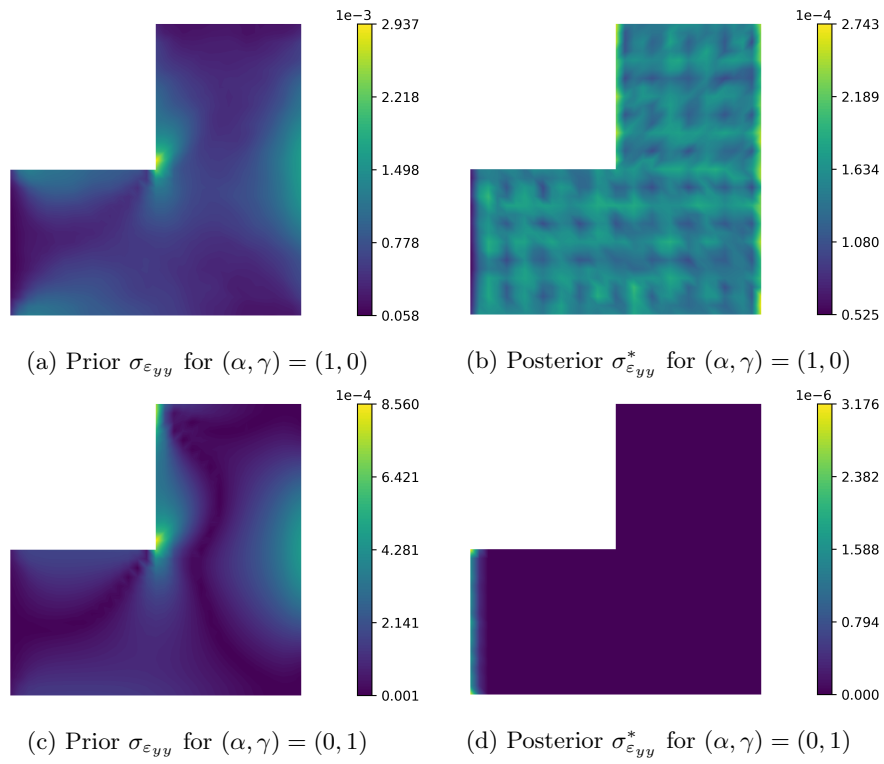


Figure 4: Prior and posterior standard deviations of the vertical strain field ( $\sigma_{\varepsilon_{yy}}$ )



$\frac{\gamma}{\alpha}$  and  $\frac{\sigma_e}{\alpha}$ , whereas the magnitude can be scaled directly using only  $\alpha$ . Additionally, under this reparametrization,  $\alpha$  no longer has any effect on the posterior mean. In Figure 5, the effects of  $\frac{\gamma}{\alpha}$  and  $\frac{\sigma_e}{\alpha}$  on the posterior mean and covariance are explored. The surface plot in the center of the figure shows the effect of the hyperparameters on the quality of the posterior mean. More specifically, the relative error between the posterior mean  $\mathbf{m}^*$  and reference solution  $\hat{\mathbf{u}}$  is plotted as a function of  $\frac{\gamma}{\alpha}$  and  $\frac{\sigma_e}{\alpha}$ .

In the region around point (a), the posterior mean is already relatively close to the reference solution, but Figure 5a shows that the singularity is not captured by the posterior covariance. If the observation noise  $\sigma_e$  increases while keeping  $\gamma$  fixed, the posterior mean tends towards the prior mean, which is zero. On the other hand, if the  $\gamma$  hyperparameter increases while keeping  $\sigma_e$  small, the posterior mean improves greatly, but the covariance still does not capture the singularity, as shown in Figure 5d. By combining both effects, however, we can strike a balance, and capture the singularity in the posterior distribution without sacrificing the quality of the posterior mean. Considering Figures 5b and 5c, we find that the addition of observation noise allows us to capture the singularity in the posterior covariance, and that the intensity of this covariance can be tuned by increasing  $\gamma$  and  $\sigma_e$  simultaneously. Finally, as shown by Figure 5e, it is possible to further improve the posterior mean without losing the structure of the posterior covariance.

### 4.3 2D porous microstructure

Finally, we consider a microscopic domain describing the microscale behavior of a heterogeneous material with randomly generated voids, shown in Figure 6. The complex geometry of this problem is known to produce strain concentrations and regions of large discretization error at multiple locations. Similar to the previous example, the focus of this example is on the strain field  $\boldsymbol{\varepsilon}(\mathbf{x})$  rather than the solution field  $u(\mathbf{x})$ . Along the left and bottom edge of the volume element, horizontal and vertical movement is restricted respectively. A unit horizontal displacement is prescribed along the right edge, and a unit vertical displacement is prescribed along the top edge. In multiscale modeling applications, this would represent a state of biaxial tension at the macroscale. Both meshes consist of triangular elements with linear shape functions, and are shown in Figure 6a. In Figure 6b, the strain field associated with the reference solution  $\varepsilon_{yy}^f$  is shown. The error in the strain field between the coarse and fine discretization  $\Delta\varepsilon_{yy} = |\varepsilon_{yy}^f - \varepsilon_{yy}^c|$  is shown in Figure 6c.

For this example, the Dirichlet boundary conditions are treated in a probabilistic manner, following Section 3.4. It is worth noting that in this specific case, the only external forces are those implied by the prescribed displacement. The prior covariance gains an additional term representing the prescribed displacement, analogous to the treatment of Neumann boundary conditions in Section 4.2:

$$\boldsymbol{\Sigma}_f = \alpha^2 \mathbf{M} + \beta^2 \mathbf{K}_{\text{id}} \boldsymbol{\Sigma}_d \mathbf{K}_{\text{id}}^T \quad (53)$$

The  $\beta$  hyperparameter takes a similar role as the  $\gamma$  hyperparameter in Section 4.2: it increases or decreases the emphasis on the effects of the boundary conditions on the discretization error.

The structure of the boundary covariance matrix  $\boldsymbol{\Sigma}_d$  depends on the assumptions that are imposed on the relation between the different nodes along the boundary. In this case, we assume that all horizontal displacements along the right edge are equal to a single value,  $u_r$ , and all vertical displacements along the top edge are equal to  $u_t$ . Both  $u_r$  and  $u_t$  are assumed to follow a standard normal distribution, and to be statistically independent. From here it follows that the entries of  $\boldsymbol{\Sigma}_d$  are equal to 1 if the row and column both correspond to a horizontal degree of freedom on the right edge, or both correspond to a vertical degree of freedom on the top edge, and 0 otherwise.

To investigate the influence of the hyperparameters, we again first consider the extreme cases  $(\alpha, \beta) = (1, 0)$  and  $(\alpha, \beta) = (0, 1)$ . The observation noise is set to a small value ( $\sigma_e = 10^{-8}$ ), so the

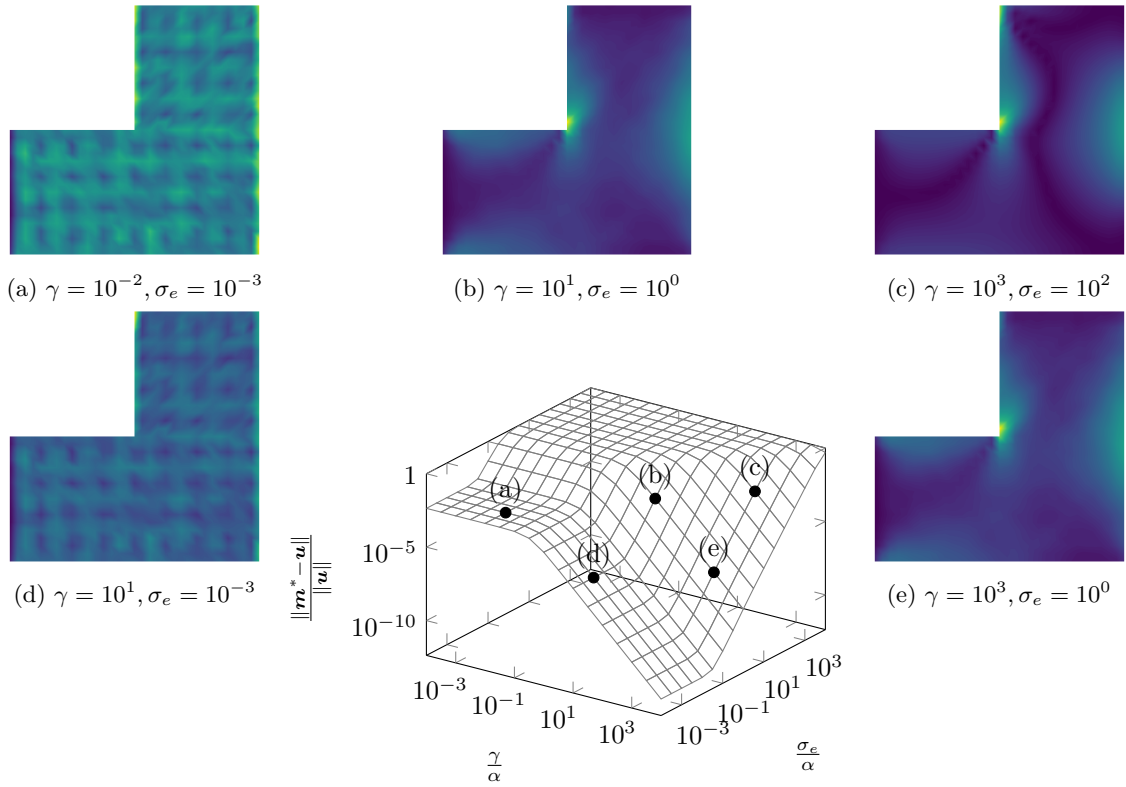


Figure 5: Comparison of the posterior mean for varying ratios of  $\frac{\gamma}{\alpha}$  and  $\frac{\sigma_e}{\alpha}$ . For some combinations of  $\frac{\gamma}{\alpha}$  and  $\frac{\sigma_e}{\alpha}$ , the posterior standard deviation of the vertical strain field is shown.

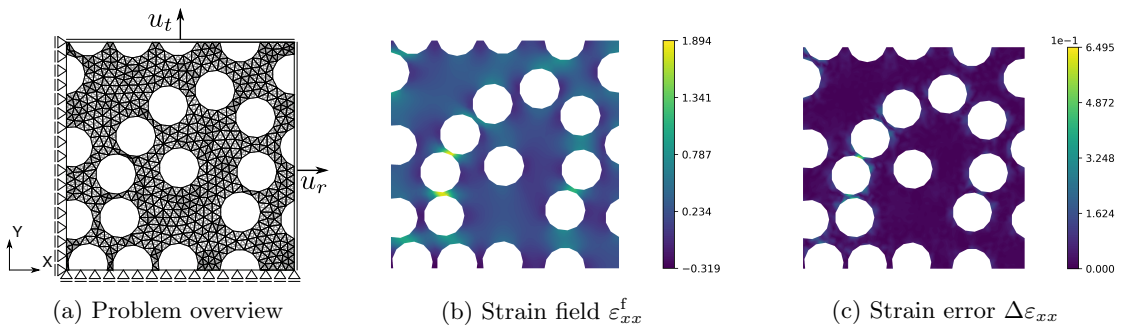


Figure 6: The vertical strain field and corresponding discretization error of the representative volume element problem

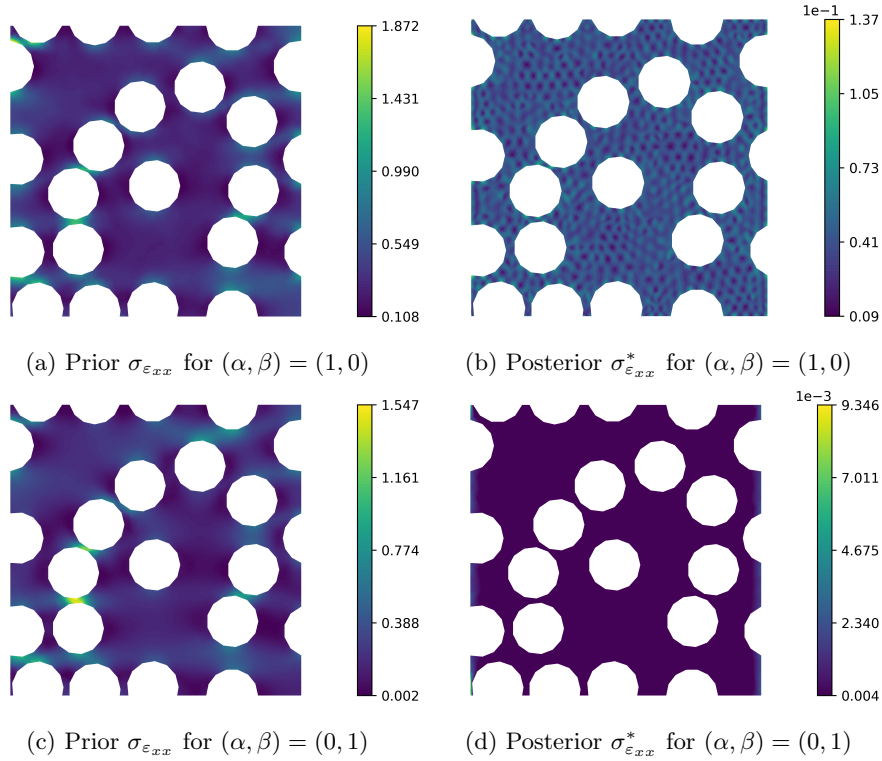


Figure 7: Prior and posterior standard deviations of the horizontal strain field ( $\varepsilon_{xx}$ )

prior and posterior distributions represent the limit cases of  $\sigma_e \rightarrow \infty$  and  $\sigma_e \rightarrow 0$ , respectively. In Figure 7, the standard deviation of the prior and posterior distributions of the strain field are plotted. Despite the problem having a very different geometry and loading conditions, clear similarities with the problem of Section 4.2 are apparent (see Figure 4). Again, it can be found that regions of strain concentrations and discretization error are already identified in the prior for  $(\alpha, \beta) = (1, 0)$ , which become more pronounced for  $(\alpha, \beta) = (0, 1)$ . In the posterior for both cases, these features are smothered by the observed data in absence of any observation noise.

In order to study the effects of the hyperparameters  $\alpha$ ,  $\beta$  and  $\sigma_e$ , the same reparametrization is performed as in Section 4.2, where only the ratios  $\frac{\beta}{\alpha}$  and  $\frac{\sigma_e}{\alpha}$  are considered, which essentially reduces  $\alpha$  to a simple scaling parameter of the prior and posterior covariance. In Figure 8, the effects of  $\frac{\beta}{\alpha}$  and  $\frac{\sigma_e}{\alpha}$  on the posterior mean and covariance are shown. Although the problem being solved is rather different from the one in Section 4.2, a remarkable similarity to Figure 5 is directly apparent. The main difference between these two figures lies in the quality of the posterior mean in the region where  $\beta \ll \alpha$  and  $\sigma_e \ll \alpha$ . This is the result of the weak enforcement of the inhomogeneous Dirichlet boundary conditions, letting them be inferred from the observed forces rather than explicitly encoded in the prior distribution. If  $\beta$  is not large enough, the displacement at the inhomogeneous Dirichlet boundary is too constrained to the prior mean. Since the prior mean is zero, they will essentially be treated as homogeneous boundary conditions, thus resulting in a large disagreement between the posterior mean and reference solution. However, given a large enough value of  $\beta$ , a posterior mean

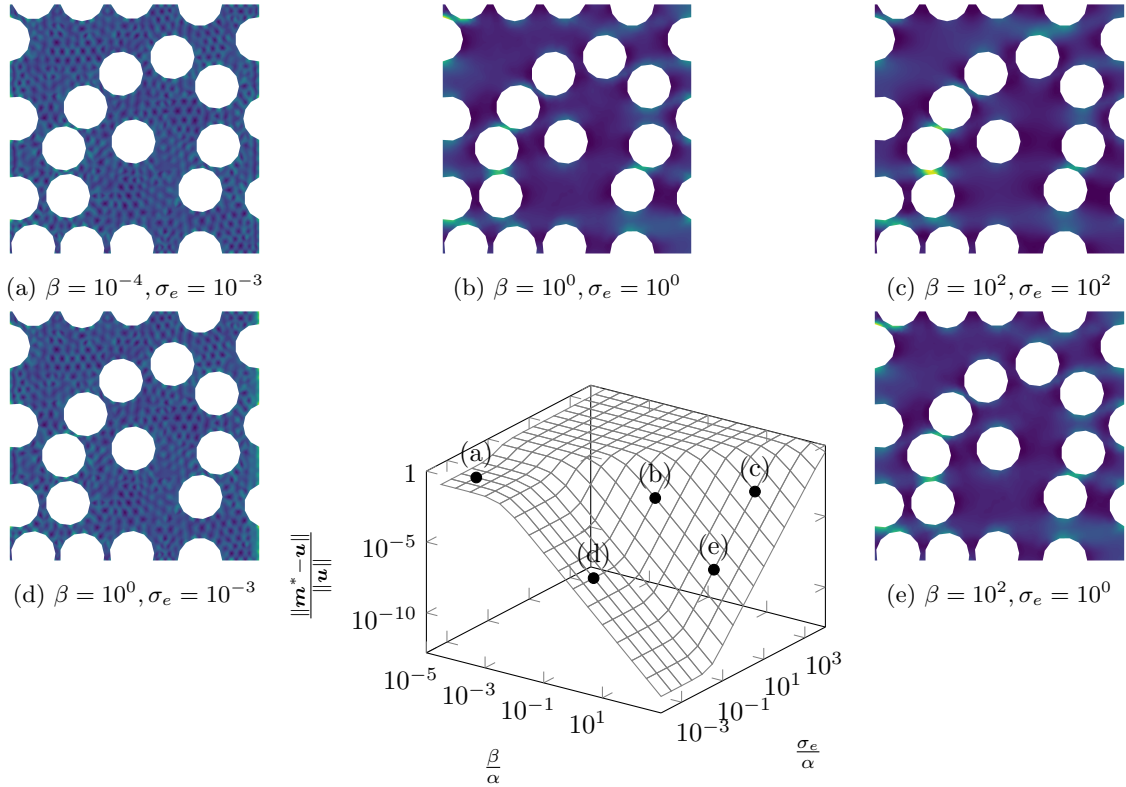


Figure 8: Comparison of the posterior mean for varying ratios of  $\frac{\beta}{\alpha}$  and  $\frac{\sigma_e}{\alpha}$ . For some combinations of  $\frac{\beta}{\alpha}$  and  $\frac{\sigma_e}{\alpha}$ , the posterior standard deviation of the vertical strain field is shown.

that is arbitrarily close to the reference solution can be obtained. Similar to the previous example, by increasing  $\sigma_e$ , regions of strain concentrations and large discretization error can be captured in the posterior covariance.

## 5 Conclusions

In this work, we presented a Bayesian approach to the modeling of finite element discretization error. Two levels of discretization are applied to the domain in a hierarchical manner, which are linked through a Petrov-Galerkin formulation. A prior distribution is assumed over the solution space of the fine discretization, which is then updated using right-hand side information from the coarse discretization only. This yields a posterior distribution with a mean that is close to the fine-scale reference solution, and a covariance representing the uncertainty due to the fact that only coarse-scale information was used to perform the update to the posterior. For the presented class of sparse right-hand side priors, a formal link between the posterior mean and fine-scale reference solution was demonstrated. Additionally, we have shown how the remaining difference between these two fields can cheaply be estimated, which is useful for determining the appropriate magnitude of the

prior covariance. The method was extended to inhomogeneous Dirichlet and Neumann boundary conditions through an additional term in the prior mean or covariance. The effects and interplay of these additional terms and observation noise were studied in detail. For 1D problems, we found that a white noise prior alone is sufficient to produce a posterior distribution with a mean that is close to the fine-scale reference solution, and a standard deviation that correctly identified regions of large discretization error. However, for 2D problems, a white noise prior alone produces a posterior standard deviation that is approximately uniform over the domain. This issue can be mitigated by including observation noise in the model, which restores the structure in the posterior covariance indicating regions of large discretization error.

One of the main drawbacks of the method we propose is its computational cost. In order to draw exact samples from the prior and posterior distribution, a fine-scale solve is needed for each sample. In future works, we will explore potential solutions to these issues by approximating or circumventing these fine-scale solves. Possible avenues of exploration include iterative solvers, Markov chain Monte Carlo sampling methods and model order reduction. A second limitation of this work is that the formulation assumes linearity on the partial differential equations and Gaussianity on the prior distribution. Extensions of the method beyond these assumptions are not trivial, though especially the extension to non-linear problems might be necessary to employ the method in practical settings. Finally, the underlying reason for the development of a Bayesian model for finite element discretization error is to allow for the consistent treatment of discretization error through computational pipelines. In this work, the focus has been on the forward problem, and the fundamentals of our Bayesian formulation of the finite element method. However, we intend to demonstrate the method in an inverse modeling context in future works.

## 6 Acknowledgements

This work is supported by the TU Delft AI Labs programme through the SLIMM AI lab. AP is thankful to Uri Peker for the fruitful discussions.

## References

- [1] A. M. Stuart. Inverse problems: A Bayesian perspective, may 2010.
- [2] Kody Law, Andrew Stuart, and Konstantinos Zygalakis. *Data assimilation: A mathematical introduction*. Springer International Publishing, sep 2015.
- [3] F. M. Larkin. Gaussian measure in hilbert space and applications in numerical analysis. *Rocky Mountain Journal of Mathematics*, 2(3):379–421, sep 1972.
- [4] Persi Diaconis. Bayesian Numerical Analysis. In J Berger and S Gupta, editors, *Statistical Decision Theory and Related Topics IV*, pages 163–175. Springer-Verlag, 1988.
- [5] Mockus J. *Bayesian Approach to Global Optimization*. Dordrecht, volume 37 of *Mathematics and Its Applications*. Springer Netherlands, Dordrecht, 1989.
- [6] A. O’Hagan. Bayes-Hermite quadrature. *Journal of Statistical Planning and Inference*, 29(3):245–260, nov 1991.
- [7] John Skilling. Bayesian Solution of Ordinary Differential Equations. In *Maximum Entropy and Bayesian Methods*, pages 23–37. Springer Netherlands, 1992.

- [8] Philipp Hennig, Michael A. Osborne, and Mark Girolami. Probabilistic numerics and uncertainty in computations. *Proceedings of the Royal Society A: Mathematical, Physical and Engineering Sciences*, 471(2179):20150142, jul 2015.
- [9] Philipp Hennig. Probabilistic interpretation of linear solvers. *SIAM Journal on Optimization*, 25(1):234–260, 2015.
- [10] Jon Cockayne, Chris J. Oates, Ilse C.F. Ipsen, and Mark Girolami. A Bayesian conjugate gradient method (with Discussion). *Bayesian Analysis*, 14(3):937–965, sep 2019.
- [11] Jonathan Wenger and Philipp Hennig. Probabilistic linear solvers for machine learning. Technical report, 2020.
- [12] Simo Särkkä, Jouni Hartikainen, Lennart Svensson, and Fredrik Sandblom. Gaussian process quadratures in nonlinear sigma-point filtering and smoothing. Technical report, 2014.
- [13] Toni Karvonen and Simo Sarkka. Classical quadrature rules via Gaussian processes. *IEEE International Workshop on Machine Learning for Signal Processing, MLSP*, 2017-September:1–6, 2017.
- [14] François Xavier Briol, Chris J. Oates, Mark Girolami, Michael A. Osborne, and Dino Sejdinovic. Probabilistic integration: A role in statistical computation? *Statistical Science*, 34(1):1–22, feb 2019.
- [15] Michael Schober, David Duvenaud, and Philipp Hennig. Probabilistic ODE solvers with Runge-Kutta means. Technical Report January, 2014.
- [16] Philipp Hennig and Søren Hauberg. Probabilistic solutions to differential equations and their application to riemannian statistics. Technical report, 2014.
- [17] Onur Teymur, Konstantinos Zygalakis, and Ben Calderhead. Probabilistic linear multistep methods. Technical report, 2016.
- [18] Oksana A. Chkrebtii, David A. Campbell, Ben Calderhead, and Mark A. Girolami. Bayesian solution uncertainty quantification for differential equations. *Bayesian Analysis*, 11(4):1239–1267, dec 2016.
- [19] Jon Cockayne, Chris Oates, Tim Sullivan, and Mark Girolami. Probabilistic Numerical Methods for Partial Differential Equations and Bayesian Inverse Problems. may 2016.
- [20] Junyang Wang, Jon Cockayne, Oksana Chkrebtii, T. J. Sullivan, and Chris J. Oates. Bayesian numerical methods for nonlinear partial differential equations. *Statistics and Computing*, 31(5):1–20, sep 2021.
- [21] M. Raissi, P. Perdikaris, and G. E. Karniadakis. Physics-informed neural networks: A deep learning framework for solving forward and inverse problems involving nonlinear partial differential equations. *Journal of Computational Physics*, 378:686–707, feb 2019.
- [22] Liu Yang, Xuhui Meng, and George Em Karniadakis. B-PINNs: Bayesian physics-informed neural networks for forward and inverse PDE problems with noisy data. *Journal of Computational Physics*, 425:109913, jan 2021.

- [23] Patrick R. Conrad, Mark Girolami, Simo Särkkä, Andrew Stuart, and Konstantinos Zygalakis. Statistical analysis of differential equations: introducing probability measures on numerical solutions. *Statistics and Computing*, 27(4):1065–1082, jul 2017.
- [24] Hans Kersting and Philipp Hennig. Active uncertainty calibration in Bayesian ODE solvers. *32nd Conference on Uncertainty in Artificial Intelligence 2016, UAI 2016*, pages 309–318, may 2016.
- [25] Han Cheng Lie, A. M. Stuart, and T. J. Sullivan. Strong convergence rates of probabilistic integrators for ordinary differential equations. *Statistics and Computing*, 29(6):1265–1283, nov 2019.
- [26] Assyr Abdulle and Giacomo Garegnani. Random time step probabilistic methods for uncertainty quantification in chaotic and geometric numerical integration. *Statistics and Computing*, 30(4):907–932, jul 2020.
- [27] Assyr Abdulle and Giacomo Garegnani. A probabilistic finite element method based on random meshes: A posteriori error estimators and Bayesian inverse problems. *Computer Methods in Applied Mechanics and Engineering*, 384:113961, oct 2021.
- [28] Jon Cockayne, Chris J. Oates, T. J. Sullivan, and Mark Girolami. Bayesian probabilistic numerical methods. *SIAM Review*, 61(4):756–789, nov 2019.
- [29] I. Babuska and W. C. Rheinboldt. Analysis of Optimal Finite-Element Meshes in R 1. Technical Report 146, 1979.
- [30] I. Babuška and A. Miller. A feedback finite element method with a posteriori error estimation: Part I. The finite element method and some basic properties of the a posteriori error estimator. *Computer Methods in Applied Mechanics and Engineering*, 61(1):1–40, mar 1987.
- [31] O. C. Zienkiewicz and J. Z. Zhu. A simple error estimator and adaptive procedure for practical engineering analysis. *International Journal for Numerical Methods in Engineering*, 24(2):337–357, feb 1987.
- [32] J P Rouse, P Kerfriden, and M Hamadi. A probabilistic hierarchical sub-modelling approach through a posteriori Bayesian state estimation of finite element error fields. Technical report, dec 2021.
- [33] Ilias Bilonis. Probabilistic solvers for partial differential equations. jul 2016.
- [34] Mark Girolami, Eky Febrianto, Ge Yin, and Fehmi Cirak. The statistical finite element method (statFEM) for coherent synthesis of observation data and model predictions. *Computer Methods in Applied Mechanics and Engineering*, 375:113533, mar 2021.
- [35] Carl Edward Rasmussen and Christopher K. I. Williams. *Gaussian Processes for Machine Learning*. MIT Press, Cambridge, MA, first edition, 2018.
- [36] Houman Owhadi. Bayesian numerical homogenization. *Multiscale Modeling and Simulation*, 13(3):812–828, 2015.
- [37] Lassi Roininen, Janne M.J. Huttunen, and Sari Lasanen. Whittle-matérn priors for Bayesian statistical inversion with applications in electrical impedance tomography. *Inverse Problems and Imaging*, 8(2):561–586, 2014.

- [38] Uri Peker. Analyzing the Influence of Prior Covariances on a Bayesian Finite Element Method. Master’s thesis, TU Delft, 2023. Awaiting publication.
- [39] Andrew C. Berry. The accuracy of the Gaussian approximation to the sum of independent variates. *Transactions of the American Mathematical Society*, 49(1):122–136, 1941.
- [40] Timothy a Davis. User Guide for CHOLMOD : a sparse Cholesky factorization and modification package. Technical report, 2013.

## A Sampling the prior and posterior

The main computational bottleneck of the method lies in the handling of large covariance matrices. Since both the prior and posterior covariance matrix are full  $n \times n$  matrices, their explicit computation, storage and handling quickly becomes infeasible as  $n$  increases. Additionally,  $\mathbf{K}^{-1}$  appears in the expressions for both of these matrices, which suffers from similar problems when computed explicitly. In this section, methods of sampling exactly from the prior and posterior distributions are discussed. From these samples, the mean vectors and covariance matrices can be approximated.

### A.1 Ensemble approximation

Instead of a mean vector and covariance matrix, an ensemble  $\mathbf{X}$  is used to represent the prior distribution.  $\mathbf{X}$  is an  $n \times N$  matrix containing  $N$  samples from the prior distribution. The prior mean and covariance can be approximated by computing the sample mean  $\hat{\mathbf{m}}$  and sample covariance  $\hat{\mathbf{\Sigma}}$  of the ensemble. The accuracy of this approximation is depends on the size of the ensemble: as  $N$  increases, the sample mean vector and covariance matrix converge to their exact counterparts, but the computational cost increases accordingly. By the central limit theorem, the sample mean and covariance will converge to the true sample mean and covariance at a rate of  $\frac{1}{\sqrt{N}}$  [39].

The entries of the sample mean vector and covariance matrix are given by:

$$\begin{aligned}\hat{\mathbf{m}}_i &= \frac{1}{N} \sum_{j=1}^N \mathbf{X}_{ij} \\ \hat{\Sigma}_{ij} &= \frac{1}{N-1} \sum_{k=1}^N (\mathbf{X}_{ik} - \hat{\mathbf{m}}_i)(\mathbf{X}_{jk} - \hat{\mathbf{m}}_j)\end{aligned}\tag{54}$$

The sample covariance matrix can also be expressed as the following decomposition:

$$\hat{\mathbf{\Sigma}} = \frac{1}{N-1} \hat{\mathbf{F}} \hat{\mathbf{F}}^T\tag{55}$$

Here,  $\hat{\mathbf{F}}$  is the sample residual matrix, given by:

$$\hat{\mathbf{F}} = \mathbf{X} - \hat{\mathbf{m}} \mathbf{1}_N^T\tag{56}$$

In the expression above,  $\mathbf{1}_N$  is a vector of ones of size  $N$ .



## A.2 Prior sampling

One key observation to make about the prior covariance in Equation (40) is that the  $\mathbf{K}^{-1}$  term only appears as a premultiplier at the front and as a postmultiplier at the end of the expression. As a result, instead of obtaining a sample  $\tilde{\mathbf{u}}$  from  $\mathbf{u} \sim \mathcal{N}(\mathbf{0}, \mathbf{K}^{-1}\Sigma_f\mathbf{K}^{-1})$ , a sample  $\tilde{\mathbf{f}}$  can be obtained from  $\mathbf{f} \sim \mathcal{N}(\mathbf{0}, \Sigma_f)$ . Since  $\Sigma_f$  is a sparse matrix, the Cholesky decomposition of  $\Sigma_f$  that is needed to sample  $\tilde{\mathbf{f}}$  is relatively cheap compared to that of a full matrix. If  $\Sigma_f$  is approximated by diagonalizing it, its Cholesky decomposition is trivial. After obtaining  $\tilde{\mathbf{f}}$ , we can compute  $\tilde{\mathbf{u}}$  by solving  $\mathbf{K}\tilde{\mathbf{u}} = \tilde{\mathbf{f}}$ .

Since multiple solves are needed of the same system, but with a changing right-hand side vector, a direct solver approach is a natural choice. Here, we use the CHOLMOD library [40], which solves sparse linear systems by finding a sparse Cholesky factorization of  $\mathbf{K}$ , and then solving for  $\tilde{\mathbf{u}}$  through backward substitution. Notice that only the cheap backward substitutions need to be repeated for each sample, and the main computational bottleneck of obtaining the factorization needs to be performed only once. Additionally, if the white-noise prior from Section 3.2 is used,  $\Sigma_f = \mathbf{M}$  and will thus have the same sparsity structure as  $\mathbf{K}$ . This means that the permutation that minimizes the fill-ins in the Cholesky decomposition of  $\mathbf{K}$  can be reused for that of  $\Sigma_f$ . One drawback of using a direct solver, however, is that it tends to scale poorly as the number of degrees of freedom in the system increases. For systems with a large number of degrees of freedom, it might therefore be necessary to find alternative sampling methods. This falls beyond the scope of this paper, but will be explored in future studies.

## A.3 Posterior sampling from $\mathbf{u}$ via $\mathbf{f}$

To obtain posterior samples with the mean and covariance from Equation (42), a similar approach can be applied. Instead of computing a posterior sample  $\tilde{\mathbf{u}}^*$  directly from  $\mathbf{u}|\mathbf{g} \sim \mathcal{N}(\mathbf{m}^*, \Sigma^*)$ , a sample of the force vector posterior  $\tilde{\mathbf{f}}^*$  is obtained, from the following distribution

$$\mathbf{f}|\mathbf{g} \sim \mathcal{N}(\mathbf{m}_{\mathbf{f}}^*, \Sigma_{\mathbf{f}}^*) \quad (57)$$

where the force posterior mean vector  $\mathbf{m}_{\mathbf{f}}^*$  and force posterior covariance matrix  $\Sigma_{\mathbf{f}}^*$  are given by:

$$\begin{aligned} \mathbf{m}_{\mathbf{f}}^* &= \Sigma_{\mathbf{f}}\Phi \left( \Phi^T \Sigma_{\mathbf{f}}\Phi + \sigma_e^2 \mathbf{I} \right)^{-1} \mathbf{g} &= \mathbf{G}_{\mathbf{f}}\mathbf{g} \\ \Sigma_{\mathbf{f}}^* &= \Sigma_{\mathbf{f}} - \Sigma_{\mathbf{f}}\Phi \left( \Phi^T \Sigma_{\mathbf{f}}\Phi + \sigma_e^2 \mathbf{I} \right)^{-1} \Phi^T \Sigma_{\mathbf{f}} &= \left( \mathbf{I} - \mathbf{G}_{\mathbf{f}}\Phi^T \right) \Sigma_{\mathbf{f}} \end{aligned} \quad (58)$$

Here,  $\mathbf{G}_{\mathbf{f}}$  is the force vector Kalman gain matrix, which is given by:

$$\mathbf{G}_{\mathbf{f}} = \Sigma_{\mathbf{f}}\Phi \left( \Phi^T \Sigma_{\mathbf{f}}\Phi + \sigma_e^2 \mathbf{I} \right)^{-1} \quad (59)$$

If the force posterior covariance matrix is written in its so-called Joseph form, it becomes clear how posterior force vector samples can be computed from prior force vector samples:

$$\Sigma_{\mathbf{f}}^* = \left( \mathbf{I} - \mathbf{G}_{\mathbf{f}}\Phi^T \right) \Sigma_{\mathbf{f}} \left( \mathbf{I} - \mathbf{G}_{\mathbf{f}}\Phi^T \right)^T + \sigma_e^2 \mathbf{G}_{\mathbf{f}}\mathbf{G}_{\mathbf{f}}^T \quad (60)$$

A prior force vector sample  $\tilde{\mathbf{f}}$ , as well as a sample  $\tilde{\mathbf{e}}$  from the observation noise  $\mathbf{e} \sim \mathcal{N}(\mathbf{0}, \sigma_e^2 \mathbf{I})$  are then drawn independently. The sample from the force vector posterior is then given by:

$$\begin{aligned} \tilde{\mathbf{f}}^* &= \mathbf{m}_{\mathbf{f}}^* + \left( \mathbf{I} - \mathbf{G}_{\mathbf{f}}\Phi^T \right) \tilde{\mathbf{f}} + \mathbf{G}_{\mathbf{f}}\tilde{\mathbf{e}} \\ &= \tilde{\mathbf{f}} + \mathbf{G}_{\mathbf{f}} \left( \mathbf{g} - \Phi^T \tilde{\mathbf{f}} + \tilde{\mathbf{e}} \right) \end{aligned} \quad (61)$$

At this point the sample from the prior distribution of the displacement field can be obtained by solving  $\mathbf{K}\tilde{\mathbf{u}}^* = \tilde{\mathbf{f}}^*$ .

#### A.4 Posterior sampling from $\mathbf{u}$ directly

This approach of computing posterior samples by updating prior samples based on perturbed observations of the data  $\mathbf{g} - \tilde{\mathbf{e}}$  can also be applied to  $\mathbf{u}$  directly. Starting from Equation (61),  $\tilde{\mathbf{f}}$  and  $\Phi^T$  can be replaced by  $\tilde{\mathbf{u}}$  and  $\mathbf{H}$ , respectively. The force vector Kalman gain matrix given in Equation (59) can be replaced by the Kalman gain matrix  $\mathbf{G}$  associated with the displacement field:

$$\begin{aligned}\mathbf{G} &= \mathbf{K}^{-1}\Sigma_f\Phi\left(\Phi^T\Sigma_f\Phi + \sigma_e^2\mathbf{I}\right)^{-1} \\ &= \Sigma\mathbf{H}^T\left(\mathbf{H}\Sigma\mathbf{H}^T + \sigma_e^2\mathbf{I}\right)^{-1}\end{aligned}\tag{62}$$

A prior sample  $\tilde{\mathbf{u}}$  is computed as described in Appendix A.2, and an independent observation noise sample  $\tilde{\mathbf{e}}$  is obtained as before from  $e \sim \mathcal{N}(\mathbf{0}, \sigma_e^2\mathbf{I})$ . The posterior sample  $\tilde{\mathbf{u}}^*$  is then given by:

$$\begin{aligned}\tilde{\mathbf{u}}^* &= \mathbf{m}^* + (\mathbf{I} - \mathbf{G}\mathbf{H})\tilde{\mathbf{u}} + \mathbf{G}\tilde{\mathbf{e}} \\ &= \tilde{\mathbf{u}} + \mathbf{G}(\mathbf{g} - \mathbf{H}\tilde{\mathbf{u}} + \tilde{\mathbf{e}})\end{aligned}\tag{63}$$

Note that this approach requires two  $\mathbf{K}\tilde{\mathbf{u}} = \tilde{\mathbf{f}}$  solves to obtain a single sample from the posterior, as opposed to the approach presented in Appendix A.3, where only a single solve is needed. One reason to still prefer the method of sampling directly from  $\mathbf{u}$  is that the final solve of  $\mathbf{K}\tilde{\mathbf{u}}^* = \tilde{\mathbf{f}}^*$  does not extend well to non-linear problems. Although non-linear partial differential equations fall beyond the scope of this paper, the option to sample directly from  $\mathbf{u}$  keeps the door open to this class of problems.